*applied sciences*

MDPI

*Article*

# Progressive Failure Mechanism and Control of Natural Pillar Groups Using Yielding Expandable Props in Continuous Mining

**Kunmeng Li [1,2,*], Yuanhui Li [1,2], Zhengchun Fu [3], Jintao Li [1,2], Yunsen Wang [1,2] and Xin Wang [1,2]**

[1] State Key Laboratory of Intelligent Deep Metal Mining and Equipment, Northeastern University, Shenyang 110819, China; neulyh@163.com (Y.L.); 2401100@stu.neu.edu.cn (J.L.); wangyunsen@mail.neu.edu.cn (Y.W.); wangx@mail.neu.edu.cn (X.W.)
[2] Institute of Deep Engineering and Intelligent Technology, School of Resources and Civil Engineering, Northeastern University, Shenyang 110819, China
[3] Hunan Research Institute for Nonferrous Metals Co., Ltd., Changsha 410100, China; 2301063@stu.neu.edu.cn
* Correspondence: likunmeng@mail.neu.edu.cn

**Abstract**

To address the challenges of high ore loss and brittle splitting of natural pillars in gently dipping and horizontal thin-vein extraction using room-and-pillar mining, a continuous, pillar-free technology that replaces natural pillars with expandable prop group, designated the room and expandable prop mining method, is investigated. In this study, the ground pressure control mechanism exerted by the expandable prop group on the stope roof is theoretically framed. Employing Universal Distinct Element Code (UDEC) numerical modeling in tandem with on-site trials, the deformation, load-bearing response, and ultimate failure of both natural pillars and expandable props, together with the progressive fracturing of the stope roof, during the extraction of gently dipping and horizontal thin veins are monitored. The novelty of this study lies in establishing a unified roof–support characteristic-curve framework for expandable prop groups, which links roof deformation, support resistance, and progressive fracture evolution and enables a direct mechanistic comparison between natural pillar groups and yielding expandable prop groups. Based on the evolution and intersections of the roof and support characteristic curves, the transition from load concentration and progressive failure of natural pillar groups to deformation accommodation and damage redistribution under expandable prop support is quantitatively characterized. The results demonstrate that expandable props permit controlled roof deformation while maintaining stable load-bearing capacity. In contrast to natural pillars, for which progressive damage develops into through-going fractures and domino-type failure, expandable prop groups redistribute roof damage toward the deeper roof and abutments, interrupt fracture coalescence, and effectively suppress progressive collapse. The revealed yielding-support mechanism provides a theoretical basis for expandable prop-group design and the implementation of continuous pillar-free mining.

**Keywords:** yielding support; expandable prop; room and pillar mining; roof characteristic curve; support characteristic curve

Check for updates

Academic Editor: Andrea Carpinteri

Received: 7 September 2026
Revised: 20 September 2026
Accepted: 21 September 2026
Published: 30 September 2026

**Copyright:** © 2026 by the authors. Licensee MDPI, Basel, Switzerland. This article is an open access article distributed under the terms and conditions of the Creative Commons Attribution (CC BY) license.

## 1. Introduction

Gently dipping thin veins account for over 30% of China's precious and non-ferrous metal reserves, and their unique geometry and shallow thickness continue to make room-and-pillar mining the dominant extraction method. To ensure safety, both continuous panel pillars and discrete point pillars (circular or rectangular) are systematically left in place.

These pillars shoulder the overburden, curb roof deflection, and preserve overall stope stability [1]. However, the attendant ore locked in these pillars, ranging from 10% to 30%, poses a direct and substantial threat to the economic viability of the operation [2–4]. In deep mining (more than 1000 m depth), high in situ stresses (30–50 MPa) and intense unloading synergistically amplify the ground pressure. Stress concentrations precipitate brittle pillar splitting or violent rock bursts, stripping the roof of its long-term self-stability capacity [5,6]. When the pillar fails, the load exerted by the roof immediately redistributes to its neighbors, amplifying their stresses and triggering successive failures, and culminating in abrupt, large-scale roof collapse, i.e., the 'domino effect' collapse. Such cascading events have already proven deadly: a single incident triggered by progressive pillar failure claimed 37 lives [7], leaving both personnel and equipment in grave danger.

Confronted with the problems of ore loss and brittle pillar failure under high stress, researchers have turned to artificial supports; roughly 50 different artificial prop designs are now commercially available. Based on their load-bearing and deformation behavior, artificial props can be divided into four categories. Brittle props, such as traditional concrete props [8,9] and sand props [10], lose their support capacity completely upon reaching ultimate strengths. Elastic–plastic props, exemplified by Can supports [10,11], maintain stable support stresses after yielding. Strain-softening props like Pumpables [12] exhibit reduced load-bearing capacity post-peak. Strain-hardening props including Omni Props [10,11] increase their load capacity during late-stage roof deformation. Although the first three categories dominate current practice, it is the strain-hardening response of the fourth that underpins the 'yielding support' concept [13]. This type is ideal for both roadways and stopes: as the roof deforms and sheds load onto the prop, the prop yields and its resistance rises while remaining stable, thereby controlling convergence without roof collapse. Li et al. [14] first introduced pre-stressed, strain-hardening expandable props to recover residual natural pillars. Its operation relies on the exothermic hydration of CaO—$CaO + H_2O \rightarrow Ca(OH)_2$—generating precisely controlled volumetric expansion. When confined, the expansion develops a controllable pre-stress against the surrounding rock mass, generating 1700 kN pre-stress [15], far surpassing the 100–500 kN of wooden wedges [16,17], mechanical devices [18,19], and pack support [20]. This pre-stress is transmitted to the roof via steel support posts and contact structures [15]. Steel posts undergo controlled compressive bending while the sleeve-type expandable structure yields axially; together they deliver strain-hardening support that peaks at 2700 kN ultimate capacity in a five-pipe assembly.

Although yielding support has proven highly effective in tunnels, as the case studies in Table 1 empirically confirm, its direct transfer to large-span stopes encounters fundamental limitations. In tunnels, confined spans foster rapid stress redistribution, whereas the extensive dimensions of stopes preclude comparable stress-relief mechanisms. Combined with the pronounced brittle-fracture tendency of natural pillars under high stress, these factors render conventional yielding support systems inadequate for gently dipping thin-vein stopes [3]. To overcome these limitations, Li et al. [21] proposed the room and expandable prop mining method, a continuous, pillar-free technology tailored for gently dipping thin-vein extraction. This method substitutes pre-stressed expandable props for pillars, eliminating ore lock-up and boosting recovery. Crucially, the expandable props activate within 20 min via a self-sustaining chemical reaction, deliver high initial loads, absorb up to 6 cm of axial compression, and can be fully installed in under two hours. Moreover, the expandable props exhibit strain-hardening under stope-roof loads, enabling the expandable props to coordinate deformation adaptively and deliver genuine yielding support. Nevertheless, the mechanism by which expandable prop group controls ground pressure and stabilizes the stope roof remains largely unexplored.

**Table 1.** Representative squeezing tunnels employing yielding support.

| Tunnel Name | Country | Reference |
|---|---|---|
| Galgenberg tunnel | Austria | Schubert [22] |
| Semmering pilot tunnel | Austria | Moritz [23] |
| Strengen tunnel | Austria | Kolymbas [24] |
| Tauern tunnel | Austria | Weidinger and Lauffer [25] |
| Koralm tunnel | Austria | Moritz [26] |
| Lötschberg Base tunnel | Switzerland | Thut et al. [27] |
| Ceneri Base tunnel | Switzerland | Merlini et al. [28] |
| Yacambú-Quibor tunnel | Venezuela | Hoek and Guevara [29] |
| Frejus tunnel | Italy–France | Panet [30] |
| Lyon-Torino Base tunnel | Italy–France | Barla et al. [31] |
| Ibbenbüren coal tunnel | Germany | Mezger et al. [32] |
| Bolu tunnel | Turkey | Dalgıç [33] |
| Enasan tunnel | Japan | Kimura et al. [34] |
| Jiazhuqing tunnel | China | Zhang [35] |
| Maoyu tunnel | China | Zhang et al. [36] |
| Dongtan coal tunnel | China | Tan et al. [37] |
| Yangshan tunnel | China | Qiu et al. [38] |

Previous studies of roof control mechanisms in room-and-pillar mining have followed three tracks: analytical models, laboratory experiments, and numerical simulations. Li et al. [39] idealized the roof as a cantilever beam and analyzed direct-shear and hinged-collapse modes, concluding that a narrowly defined support force is indispensable for stability. Guo and Miao [5] employed thin-plate theory to derive roof-deflection equations, establishing a quantitative relationship between pillar dimensions and the redistribution of induced stresses. The theoretical models oversimplify the rock mass heterogeneity and invoke boundary conditions that seldom prevail in situ. Crucially, existing theoretical frameworks lack unified assumptions and hinge on empirical parameter fitting. Lu et al. [40] performed true-triaxial tests that replicated coal-seam extraction, quantifying the full stress–deformation–failure evolution during excavation. Guo et al. [3] conducted large-scale physical simulations of NPR-bolt-supported stopes, capturing real-time stress redistribution and fracture development. These tests are constrained by the fact that multi-physics scaling compromises similarity, boundary conditions fall short of replicating the true field environment, and extrapolation falters in the face of nonlinear rock response. Numerical simulation more flexibly and conveniently provides the deformations of the rock mass around excavations under various support forces for the roof characteristic curve. Two dominant numerical simulation methods are continuum-based and discontinuum-based methods. Bai et al. [41] used FLAC3D to reveal that the central deflection of the roof governs deformation throughout the surrounding rock mass. Kong et al. [42] simulated roof failure under varying support loads to determine the optimal support strength for roof stability by Distinct Element Code (UDEC) modeling; subsequent field implementation proved effective in eliminating face-end falls. Compared with the Finite Element Method (FEM) and Finite Difference Method (FDM), the Discrete Element Method (DEM) captures rock mass fracturing and failure without the need for fine meshes or sophisticated constitutive models [43]. As a leading discrete element code, the UDEC [44] constructs an equivalent rock mass model that faithfully replicates the physical behavior observed in situ. In the UDEC, block models govern intact rock behavior, and contact models govern joint and fracture mechanics. Gao and Stead [45] advanced the UDEC-Trigon approach, discretizing rock masses into interacting triangular blocks. This approach allows for direct visualization of progressive failure via block rotation and crack propagation, offering unrivaled fidelity in modeling brittle excavation responses in jointed rock masses.

This study introduces a continuous, pillar-free method for extracting gently inclined thin veins, i.e., the room and expandable prop mining method, in which the expandable prop group carries the entire roof load. The 'yielding support' mechanism by which the expandable prop group controls stope roof ground pressure is theoretically established. Using UDEC simulations and in situ trials, the deformation, load-bearing responses, and failure of both natural pillars and expandable props, together with the progressive failure of the stope roof, are monitored throughout the extraction of gently and horizontally inclined thin veins. By comparing the intersections of the roof and support characteristic curves, the 'yielding support' mechanism through which the expandable prop group controls roof ground pressure in room and expandable prop mining is elucidated and quantified.

## 2. A Continuous, Pillar-Free Method for Extracting Gently Inclined Thin Veins

To counter the high ore losses, recurring ground pressure hazards, and limited production capacity inherent in conventional room-and-pillar mining (Figure 1a), a continuous, pillar-free technology for gently inclined thin veins, the room and expandable prop mining method, is proposed, wherein an integrated array of pre-stressed expandable props wholly replaces natural pillars to carry the roof load. As illustrated in Figure 1b, the stope is no longer subdivided into rooms and intervening pillars; instead, a continuous zonal strip of prescribed span serves as the mining unit, enabling single-pass, strike-continuous extraction. Relative to the conventional room-and-pillar mining method, the stope span is more than doubled for the room and expandable prop mining method, from 16 m to over 45 m. A V-shaped working face is adopted to collect and convey blasted ore; the enlarged stope span and higher haulage capacity lift the daily output to 80–100 t. Shallow hole blasting is adopted, and no natural pillars are left in the stope, while the pre-stressed expandable props are erected to reduce the loss of the ore resources, where the loss rate is about 5–10%. A filling-isolation curtain is installed at the boundary of every mining sub-district to allow cemented tailings backfill in the goaf. The expandable prop group and cemented tailings together create a composite backfill, and the stope roof is carried primarily by the expandable props. Therefore, the binder content in the backfill can be lowered, cutting filling costs. A top-down mining sequence is employed both between stages and within each stope, transferring high stresses to the unmined zones and eliminating the safety hazards inherent in bottom-up extraction. The accumulated high stress is harnessed to pre-fracture the unmined orebody, improving fragmentation and cutting specific explosive consumption. Field trials of the room and expandable prop mining in gently dipping thin veins demonstrate the method's excellent performance (Figure 1b). Relative to conventional room-and-pillar mining (Figure 1a), the new technique ensures superior stope stability and eliminates catastrophic roof-collapse risk. However, the underlying support mechanism by which the expandable prop group stabilizes the stope roof remains the key scientific premise for the wider adoption of room and expandable prop mining.

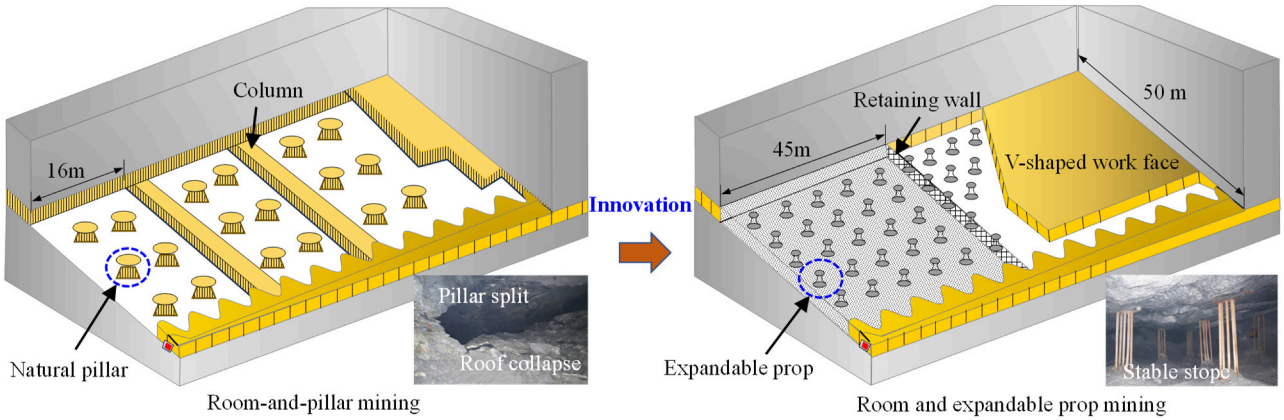



**Figure 1.** Design and field application of room and expandable prop mining for gently inclined thin veins: (**a**) traditional room-and-pillar mining method; (**b**) room and expandable prop mining method.

## 3. Theoretical Support Mechanism of Expandable Prop Group to Stope Roof

While Li et al. [14] clarified the support behavior of a single expandable prop, the theoretical support mechanism of expandable prop group in governing stope roof stability during room and expandable prop mining for gently inclined thin veins remains to be elucidated. The collective support performance of natural pillars, expandable prop groups, and conventional concrete props is compared. Because natural pillars engage the roof almost immediately, their support characteristic curve ① intersects the roof characteristic curve ③ at an early stage (point *a* in Figure 2), locking the stope roof into a stable state. Current designs err on the side of caution, employing both more and larger pillars than strictly necessary; while this guarantees stope stability, it locks a substantial tonnage of ore in place. To provide yielding support and maximize ore recovery, both the quantity and dimensions of the natural pillars are sharply reduced. As time elapses, spans widen, or latent defects surface, the failure of one pillar can trigger a 'domino effect' collapse for the pillar group; the roof and support characteristic curves then diverge (line ② and line ④ in Figure 2), precipitating large-scale roof fracture. Traditional concrete props, despite their high individual capacity (25 MPa (Cao et al. [8])), cannot make effective contact with the roof. Moreover, their installation cycle is protracted, so the support implementation lags behind excavation-induced roof movement. The roof characteristic curve ③ intersects the concrete prop support curve ⑥ at point *d* (Figure 2) before the roof has deformed enough to engage the props' full capacity. As time passes or the stope span widens, the props take on more load, and deformation accelerates. Either brittle failure of a single concrete prop or roof deformation beyond its limit can trigger a 'domino effect' collapse; the roof characteristic and concrete prop support characteristic curves diverge (lines ④ and ⑥ in Figure 2), precipitating catastrophic stope instability.

Although the expandable prop group engages the roof later than natural pillars, its active support capability activates it well ahead of the delayed response typical of concrete props. Pre-stressed expandable props exhibit strain-hardening load capacity and accommodate substantial deformation. As time progresses or the stope span widens, the roof and support characteristic curves for the expandable prop are always intersect (points *b* and *c* of line ④ and ⑤), ensuring continuous stope stability. Overall, relative to natural pillars, the roof deforms further, and the loads carried by the expandable prop group remain markedly lower (Figure 2), confirming that the pre-stressed expandable props deliver true 'yielding support' to the stope roof.

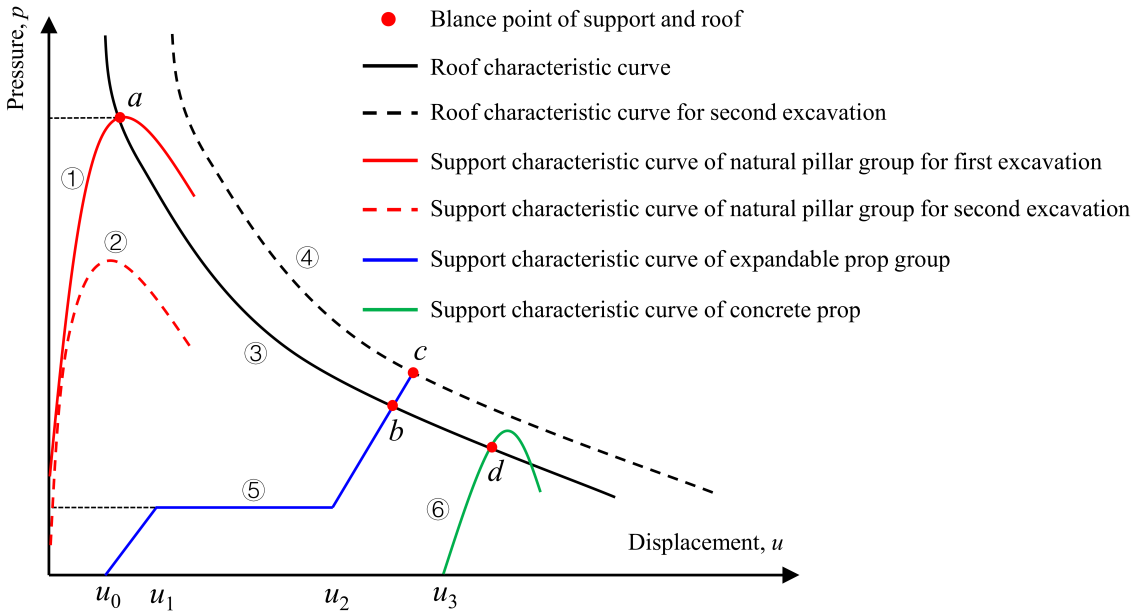



**Figure 2.** Theoretical support mechanism of expandable prop group to the stope roof.

## 4. Numerical Simulation Conditions

### *4.1. Numerical Model*

As shown in Figure 3, to maximize efficiency, using the UDEC simulation, the model captures only the discontinuous rock mass around the stope, using triangular blocks and their contacts. The 2D model couples a continuum exterior with a discrete interior, measuring 140 m × 200 m overall, and uses 0.5 m triangular blocks. The study targets a 4 m thick, sub-horizontal (0° dip) gold vein in Dandong, China, developing support designs for both a single pillar or prop and pillar or prop group, with modeling at 2 m in width and 4 m in height. Extraction advances from the center toward both flanks, with natural pillars or expandable props installed at a height of 68 m from the bottom of the numerical model. The bottom boundary is fixed, while the lateral boundaries are constrained in the horizontal direction. The bottom boundary of the numerical model corresponds to a burial depth of 400 m. Because the model is 140 m high, the upper boundary corresponds to a burial depth of 260 m. The vertical in situ stress induced by the overlying rock mass is expressed as $S_V = \rho g H = \gamma H$, where $\rho$ is the average density of the overlying rock mass, $g$ is the gravitational acceleration, $H$ is the burial depth, and $\gamma = \rho g$ is the unit weight of the rock mass. Following Ref. [46], an average unit weight of approximately 27 kN/m$^3$ is adopted. After unit conversion, the vertical stress in MPa can therefore be expressed as $S_V = 0.027H$. The horizontal in situ stress is estimated according to Ref. [46] as $S_H = (150/H + 1.4)S_V$, where $S_H$ is the horizontal in situ stress. At the model bottom, corresponding to a burial depth of 400 m, $S_V$ = 10.8 MPa, and $S_H$ = 19.17 MPa. Accordingly, the equivalent vertical stress applied to the upper boundary of the model is $S_{V\text{-top}} = 0.027 \times (400 - 140) = 7.02$ MPa. The stope floor is located 68 m above the model bottom, and the stope height is 4 m. Therefore, the stope roof is located 72 m above the model bottom, corresponding to a burial depth of 328 m. The initial vertical stress at the stope roof is thus $S_{V\text{-roof}} = 0.027 \times (400 - 72) = 8.856$ MPa.

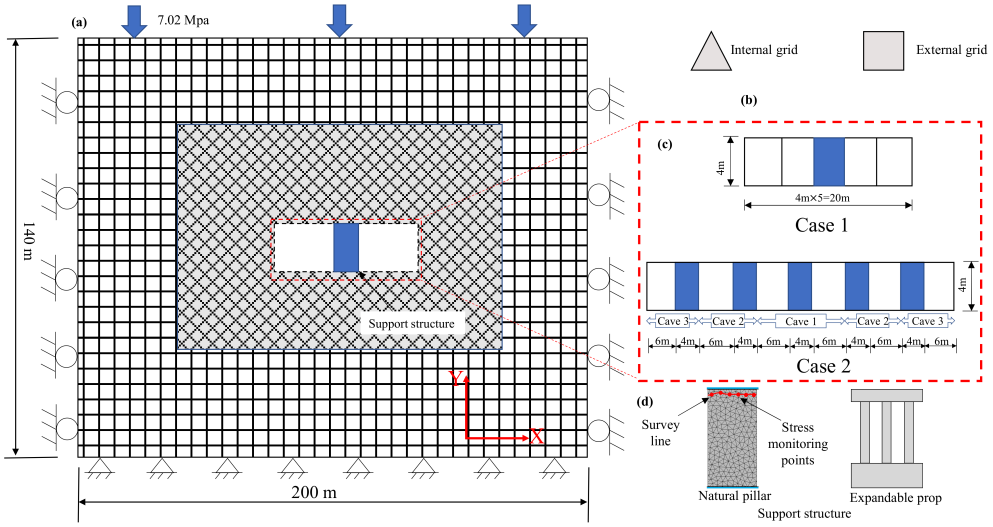



**Figure 3.** Model and monitoring layout: (**a**) numerical model, (**b**) meshing, (**c**) mining design, and (**d**) supporting structures.

### *4.2. Simulation Parameters*

Laboratory tests and field surveys feed the Hoek–Brown criterion to determine the mechanical parameters of intact rock and rock mass parameters listed in Table 2. The model represents the rock mass as an outer continuum encasing an inner, explicitly discontinuous zone. The outer continuum is assigned the rock mass parameters directly. Within the inner discontinuum, the UDEC's Trigon logic renders the rock mass as an assembly of deformable triangular blocks linked by explicit contacts [43,47]. Within the equivalent rock mass, each triangular block is treated as an elastic solid with the same mechanical properties as intact rock. The mechanical interactions between the triangular blocks are governed by Coulomb's friction law. Contact surfaces between blocks can fail in shear or tension according to their strength, as shown in Figure 4.

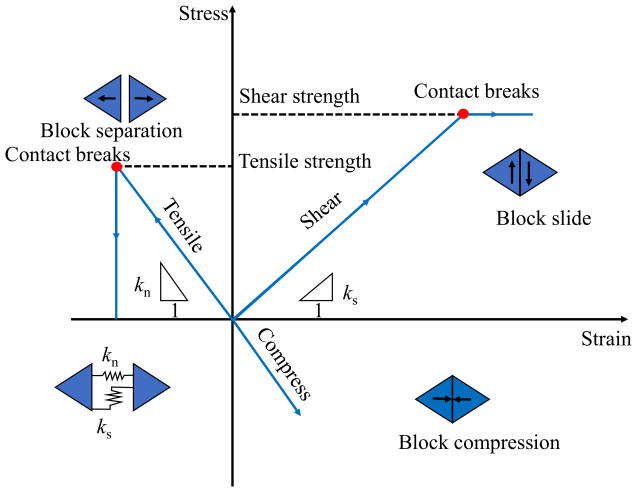



**Figure 4.** Failure mechanism of block contact.

**Table 2.** Mechanical parameters of intact rock and rock mass.

| Property | Density $\rho$ (g/cm$^3$) | Uniaxial Compressive Strength $\sigma_c$ (MPa) | Young's Modulus $E$ (GPa) | Poisson's Ratio $u$ | Cohesion $c$ (MPa) | Friction Angle $\varphi$ (°) | Tensile Strength $\sigma_t$ (MPa) |
|---|---|---|---|---|---|---|---|
| Intact rock | 2.70 | 98.16 | 54.04 | 0.23 | 14.65 | 38.6 | 5.11 |
| Rock mass | 2.70 | 17.63 | 28.54 | 0.23 | 3.14 | 35.0 | 1.63 |

Normal stress and displacement across each contact are taken as linear, governed by normal stiffness $k_n$:

$$\Delta\sigma_n = -k_n \times \Delta\mu_n \quad (1)$$

where $\Delta\sigma_n$ and $\Delta\mu_n$ denote the normal stress and displacement increments, respectively. If the normal stress $\sigma_n$ exceeds the tensile strength, $\sigma_n$ is set to 0.

In the shear direction, the mechanical response of the triangle is controlled by the constant shear stiffness ($k_s$), and the shear stress ($\tau_s$) is determined by the contact characteristics, cohesive ($c$) and frictional ($\varphi$).

$$|\tau_s| \leq c + \sigma_n \times \tan\varphi = \tau_{max} \quad (2)$$

Then,

$$\Delta\tau_s = -k_s \times \Delta\mu_n^e \quad (3)$$

or else, if $|\tau_s| \geq \tau_{max}$, then

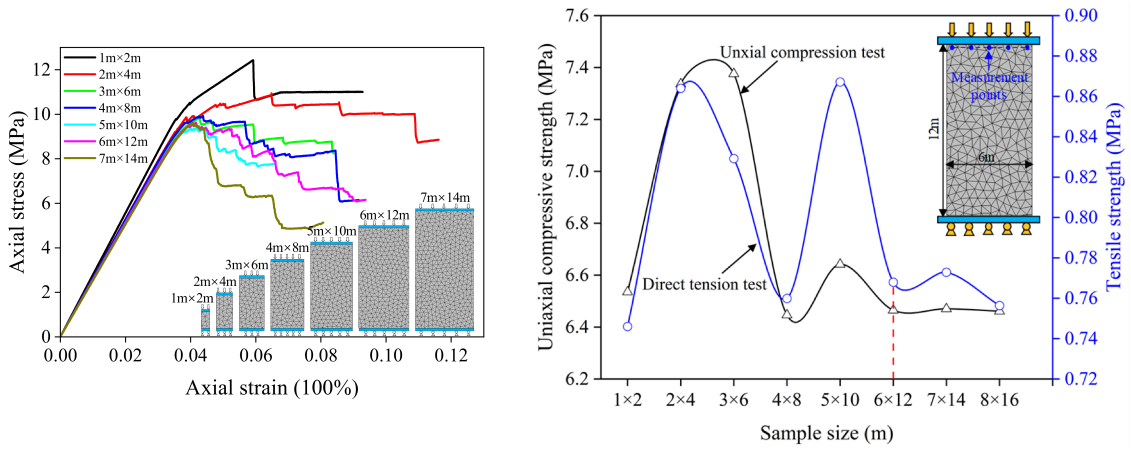
$$\tau_s = \text{sign}(\Delta\mu_n^e) \times \tau_{max} \quad (4)$$

where $\Delta\mu_n^e$ is the elastic portion of the incremental shear displacement, $\Delta\mu_s$ is the total incremental shear displacement, and $\tau_{max}$ represents the shear strength.

In the UDEC-Trigon model, a local crack is generated when a block contact reaches either the tensile failure criterion or the Mohr–Coulomb shear failure criterion. With continued excavation and stress redistribution, failed contacts progressively propagate and coalesce. A through-crack is considered to form when adjacent failed contacts develop into a continuous connected fracture path across the load-bearing roof zone.

Contact parameters for the discrete blocks are obtained by inversion. Equivalent rock mass specimens are established and subjected to uniaxial compression and tension tests to obtain their uniaxial compressive strength, elastic modulus, tensile strength, and other key parameters; contact properties are then back-calibrated to match in situ rock mass behavior. The equivalent rock mass specimen exhibits a pronounced size effect, i.e., its mechanical parameters vary with specimen dimensions. A sensitivity analysis of specimen size is therefore required to determine the representative unit before contact parameters are calibrated. The triangular blocks are fixed at 0.5 m, and equivalent rock mass specimens are prepared with a 2:1 width-to-height ratio. Specimens are modeled at 1 × 2 m, 2 × 4 m, 3 × 6 m, 4 × 8 m, 5 × 10 m, 6 × 12 m, and 7 × 14 m. The mechanical parameters of the blocks are derived from those of the rock. However, the contact mechanical parameters between blocks are adjusted within a specific range. Uniaxial compression tests are run with the base fixed and the top boundary velocity-controlled at 0.001 m/s. As shown in Figure 5, the stress–strain curves of equivalent rock masses with different sizes are obtained. Beyond 6 × 12 m, further size increases have a negligible effect (Figure 5); the 6 × 12 m specimen is therefore taken as the representative unit.

Contact parameters between the blocks are then calibrated. Considering the normal stiffness $k_n$, the shear-to-normal stiffness ratio $k_s/k_n$, cohesion $c_j$, internal friction angle $\varphi_j$ and tensile strength, 49 orthogonal experiments with 6 factors and 7 levels are designed, as shown in Table 3. Mechanical parameters of blocks are taken directly from the rock. For each project, uniaxial compression and tension experiments are conducted to obtain the mechanical parameters of the rock mass, including uniaxial compressive strength ($\sigma_c$), elastic modulus ($E$), Poisson's ratio ($u$), and tensile strength ($\sigma_t$). A sensitivity analysis is also carried out to assess how variations in the contact parameters influence the overall rock mass response.




(**a**) (**b**)

**Figure 5.** Sensitivity analysis of the equivalent rock mass size: (**a**) stress–strain curves of equivalent rock masses with different sizes; (**b**) variation law of mechanical properties of multi-scale sample models.

**Table 3.** Orthogonal tests of contact parameter calibration in numerical model.

| Levels | $k_n$ (GPa) | $k_s/k_n$ | $c_j$ (MPa) | $\varphi_j$ (°) | $\sigma_{tj}$ (MPa) |
|---|---|---|---|---|---|
| 1 | 20 | 0.2 | 0.5 | 15 | 0.2 |
| 2 | 50 | 0.3 | 1.0 | 20 | 0.5 |
| 3 | 100 | 0.4 | 2.0 | 25 | 0.8 |
| 4 | 150 | 0.5 | 3.0 | 30 | 1.0 |
| 5 | 200 | 0.6 | 4.0 | 35 | 1.5 |
| 6 | 250 | 0.7 | 5.0 | 40 | 2.0 |
| 7 | 300 | 0.8 | 6.0 | 45 | 2.5 |

A correlation coefficient matrix linking contact and rock mass parameters is plotted in Figure 6. The correlation between contact parameters and rock mass properties is further analyzed via uniaxial compression and tension tests on rock mass specimens. The uniaxial compressive strength ($\sigma_c$) of the rock mass is closely related to the block contact's cohesion ($c_j$) and internal friction angle ($\varphi_j$). The elastic modulus $E$ of the rock mass largely depends on the contact normal stiffness $k_n$ and the shear-to-normal stiffness ratio $k_s/k_n$ of the block contact. The rock mass's Poisson's ratio ($\nu$) is mainly determined by the block contact's shear-to-normal stiffness ratio ($k_s/k_n$). The rock mass's tensile strength ($\sigma_t$) is linked to the block contact's tensile strength ($\sigma_{tj}$).

Using a multi-nonlinear regression model [48,49], the rock mass's mechanical parameters and the block's contact mechanical parameters are fitted, as shown in Figure 7. The mechanical parameters of the rock mass and the contact mechanical parameters of the block exhibit nonlinear relationships. The uniaxial compressive strength ($\sigma_c$), internal friction angle ($\varphi_j$), and cohesion ($c_j$) are inter-related, while the elastic modulus ($E$) correlates with the normal stiffness ($k_n$) and the shear-to-normal stiffness ratio ($k_s/k_n$). Poisson's ratio ($\nu$) correlates with the normal stiffness ($k_n$) and the shear-to-normal stiffness ratio ($k_s/k_n$). The tensile strength ($\sigma_t$) of the rock mass and the contact tensile strength ($\sigma_{tj}$) of the block contact exhibit an approximately linear relationship. Predictions from the machine learning model [49,50] are in close agreement with UDEC calibration values. The machine learning model reliably links microscopic contact parameters to macroscopic rock mass behavior. Matching prototype rock mass mechanical properties yields the calibrated the mechanical parameters of block contacts in the UDEC model (Table 4). The calibrated rock mass properties show good agreement with the target values, with absolute relative errors below 4% (Table 5).

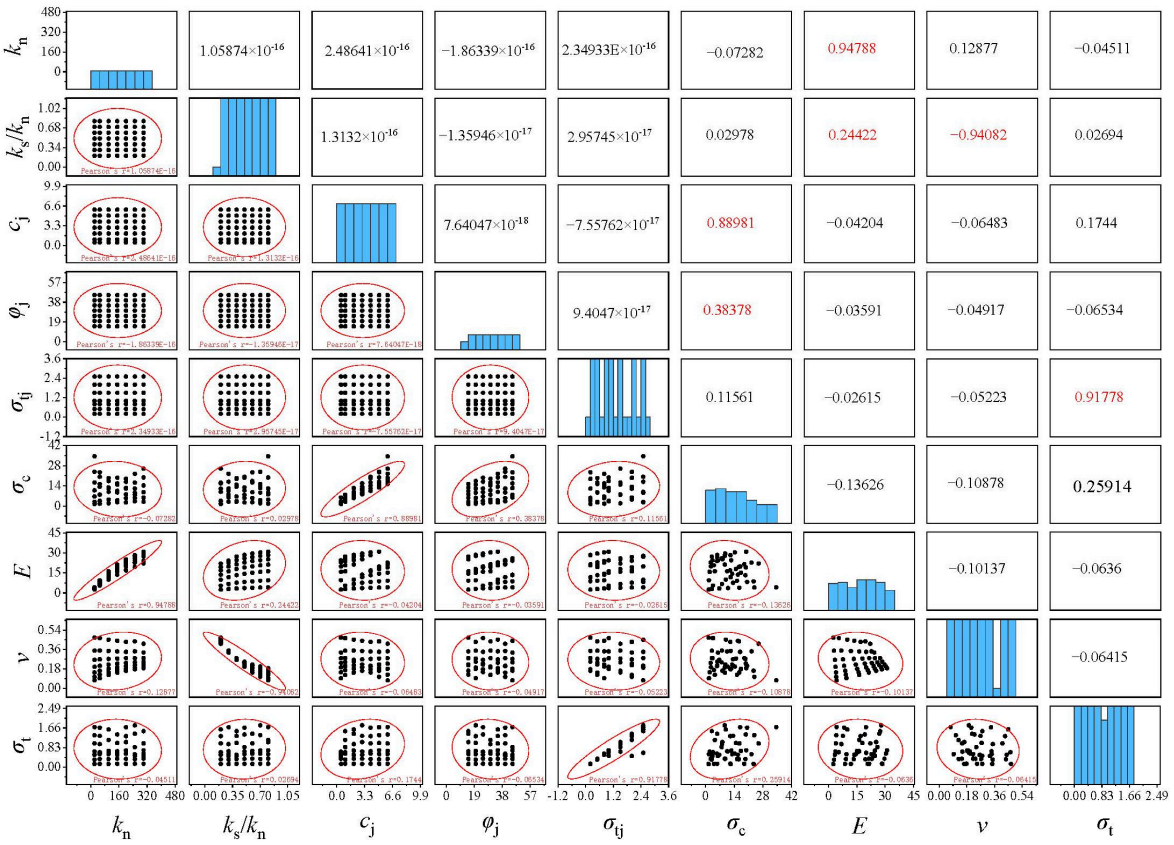



**Figure 6.** Correlation coefficient matrix of contact parameters and rock mass parameters.

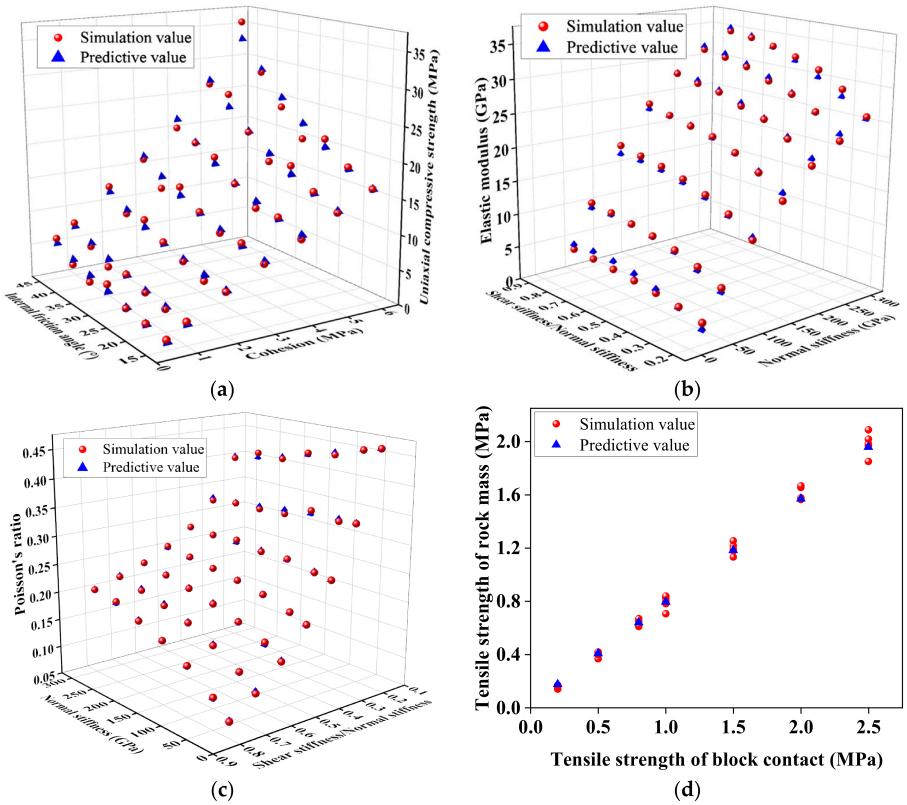



**Figure 7.** Fitting results of rock mass mechanical parameters and block contact parameters: (**a**) uniaxial compressive strength, (**b**) elastic modulus, (**c**) Poisson's ratio, and (**d**) tensile strength.

**Table 4.** Mechanical parameters of block and contact in numerical model.

| Block | | | Contact | | | | |
|---|---|---|---|---|---|---|---|
| $\rho$ (g/cm$^3$) | $E$ (GPa) | $u$ | $k_n$ (GPa) | $k_s$ (GPa) | $c_j$ (MPa) | $\varphi_j$ (°) | $\sigma_{tj}$ (MPa) |
| 2.7 | 54.04 | 0.23 | 200.0 | 100.0 | 4.0 | 30.0 | 2.0 |

**Table 5.** Calibrated rock mass properties in the Trigon model.

| $\sigma_c$ (MPa) | | | $E$ (GPa) | | | $\sigma_t$ (MPa) | | |
|---|---|---|---|---|---|---|---|---|
| Target | Calibrated | Error (100%) | Target | Calibrated | Error (100%) | Target | Calibrated | Error (100%) |
| 17.63 | 17.85 | 1.23 | 28.55 | 27.94 | −2.14 | 1.63 | 1.69 | 3.68 |

### *4.3. Monitoring Layout*

Roof displacements are extracted for varying excavation spans and support forces to construct the roof characteristic curves. Displacements are monitored at the center of the goaf, as shown in Figure 8a. For the natural pillar (Figure 8b), the deformation monitoring points are set on the stope roof, and the stress monitoring points are set in the middle of the natural pillar so as to obtain its support characteristic curve. Because neither natural pillars nor expandable props cover the entire roof, their measured loads must be averaged across the full roof span; the recorded stresses are therefore divided by the ratio of the total roof area to the actual support area to obtain the true support characteristic curves.

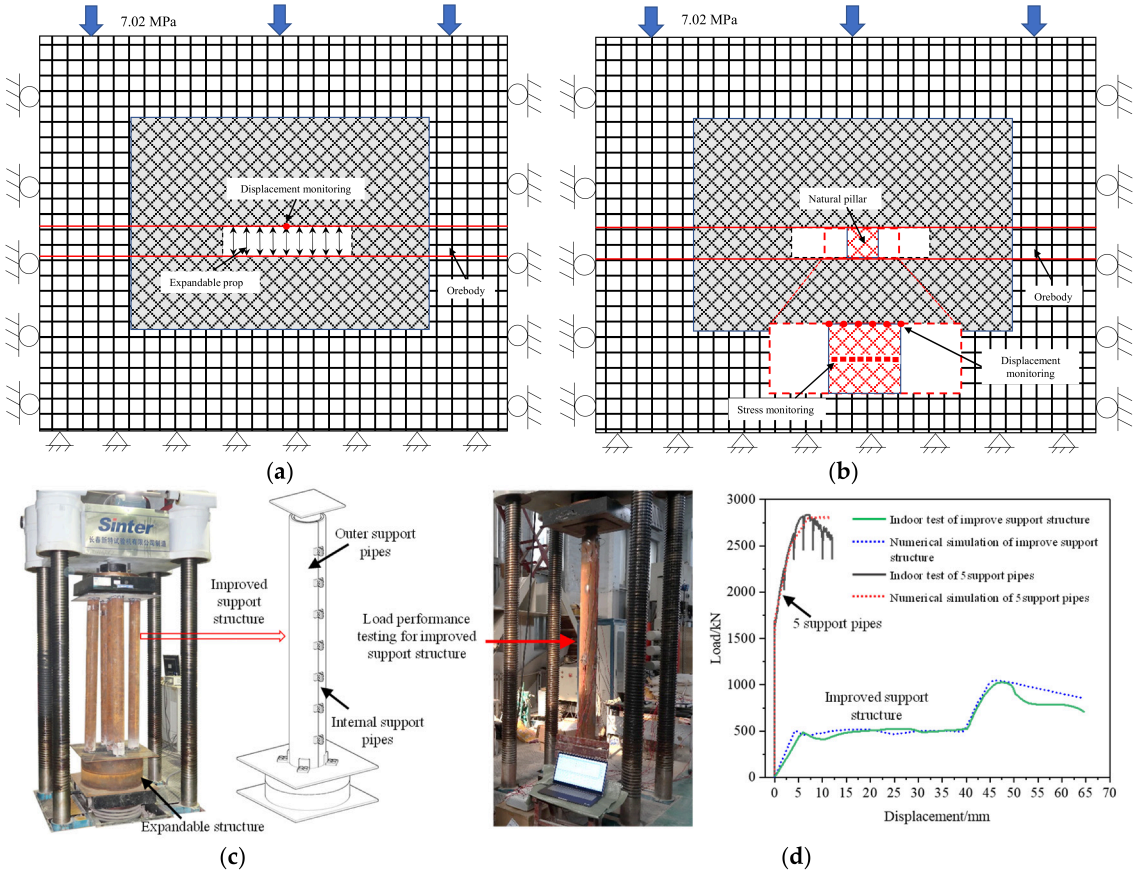



**Figure 8.** Monitoring design: (**a**) acquisition of roof characteristic curves, (**b**) the monitoring design for the natural pillar, (**c**) improved expandable prop, and (**d**) load bearing and deformation curves of the expandable prop.

Numerical simulations are conducted for room and natural pillar and expandable prop mining under four support scenarios: (i) single natural pillar, (ii) single expandable

prop, (iii) natural pillar group, and (iv) expandable prop group. As shown in Figure 8c, a structural improvement is presented and tested on the basis of the previous structure of the expandable prop [15]. The improved expandable prop's constitutive model, derived from laboratory load-deformation tests, is coded into the simulation (Figure 8d). The upgraded expandable prop delivers large deformation (about 50 mm) and high bearing capacity (up to 4 500 kN) while enabling secondary strengthening. In the improved expandable prop scenarios, the load-deformation histories are recorded to generate the corresponding support characteristic curve.

## 5. Results and Analysis

Section 5 presents four numerical simulation cases: a single natural pillar, a single expandable prop, a natural pillar group, and an expandable prop group. These are deterministic UDEC simulations rather than repeated physical experiments. The simulations were performed through progressive excavation stages, and the main outputs include support stress–deformation responses, roof displacement, crack distributions, and fracture indices. For the group support cases, three principal excavation stages were simulated; additional re-equilibration steps were performed after failed natural pillars were removed.

### *5.1. A Single Support*

#### 5.1.1. Natural Pillar

For a single support of the natural pillar with a modest 12 m span, i.e., first excavation, the roof characteristic curve is drawn in line ④ in Figure 9. The monitored stress–deformation response of the natural pillar is plotted as line ① in Figure 9, i.e., the support characteristic curve, intersecting the roof curve at point *a*. It is worth emphasizing that the pillar's stress–deformation curve has been scaled by the ratio of its cross-sectional area to the total support zone area. This scaling is based on force equilibrium over the tributary roof area, and the equivalent support pressure is expressed as $p_s = \sigma_p A_p / A_t$), where $\sigma_p$ is the axial stress of the natural pillar, $A_p$ is the pillar cross-sectional area, and $A_t$ is the tributary roof area supported by the pillar. The equilibrium state of the roof–pillar system is determined by the intersection of the roof characteristic curve and the pillar support characteristic curve. The stope roof is located 72 m above the model bottom and therefore corresponds to a burial depth of 328 m. According to $S_V = 0.027H$, the initial vertical stress at the stope roof is 8.856 MPa. After scaling the pillar stress by the ratio of the pillar cross-sectional area to the tributary support area, the equivalent initial support stress is 8.856/3 = 2.952 MPa. Minor cracking appears in both the stope roof and the natural pillar, as shown in Figure 10a. This confirms that a 12 m span supported by a single natural pillar keeps the stope roof stable. As the excavation span widens, the roof characteristic curve shifts rightward, as drawn in lines ⑤ and ⑥. Consequently, the stress–deformation curve is rescaled in proportion to the larger roof area borne by the natural pillar. If mining proceeds further, the roof characteristic curve continues its rightward shift until it intersects the pillar support characteristic curve ② precisely at the peak strength point of the stress–deformation curve of the natural pillar ⑤, as shown by point *b*. Once the natural pillar attains its peak load, cracking intensifies, as depicted in Figure 10b,c. At this stage, the pillar is effectively unstable; it is therefore removed from the model. The model is re-equilibrated at the same span, yielding an unsupported roof deformation of 11.8 mm, shown as the intersection point *c* of lines ③ and ⑥ in Figure 9. The final fracture pattern is shown in Figure 10d; cracks fully penetrate the roof, confirming its imminent collapse.

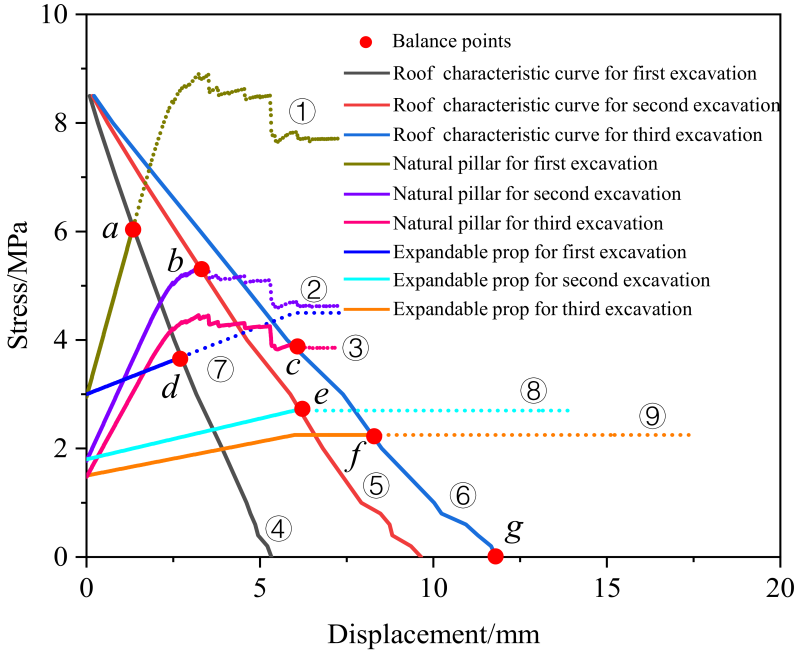



**Figure 9.** Interaction of roof and support characteristic curves for a single natural pillar and a single expandable prop.

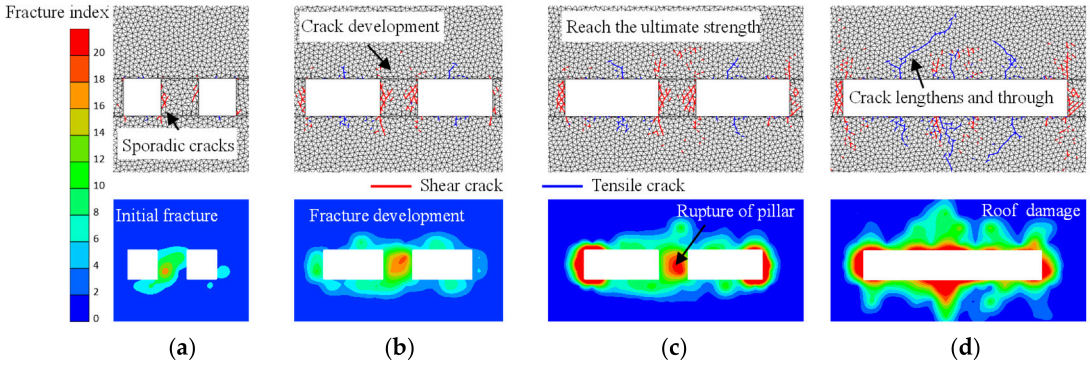



**Figure 10.** Final crack and fracture distribution supported by a single natural pillar support: (**a**) first excavation, (**b**) second excavation, (**c**) reaching the ultimate strength of natural pillar, and (**d**) the final stope state after deleting the natural pillar.

Cumulative shear and tensile crack lengths are extracted with the UDEC's built-in FISH to quantify the fracturing degree of the surrounding rock mass. A fracture index $D$ is introduced:

$$D = (L_s + L_t)/L_c \quad (5)$$

where $L_s$ is the cumulative length of shear cracks, $L_t$ the cumulative length of tensile cracks, and $L_c$ the total length of block contacts in the model.

As shown in Figure 10a, the natural pillar exhibits only minor fracturing and remains well below its ultimate strength, with a maximum fracture index $D$ of merely 9.2%. Figure 10b,c show increasingly dense cracking within the natural pillar. Once the fracture index $D$ exceeds 20%, the pillar is considered fully ruptured and no longer capable of sustaining load. It should be noted that the critical value of $D$ = 20% is used to identify the global rupture of the natural pillar rather than the formation of a through-crack in the stope roof. Roof through-cracking is identified by the formation of a continuous connected path of failed contacts. After the failed pillar is removed, cracks progressively coalesce and propagate through the stope roof (Figure 10d), indicating imminent roof collapse.

5.1.2. Expandable Prop

For a single expandable prop occupying the same support area, when the stope span is set at 12 m, identical to the initial excavation for the natural pillar, the expandable prop's support characteristic curve intersects the roof characteristic curve at point *d* on lines ④ and ⑦ in Figure 9. The expandable prop stabilizes the stope roof, evidenced by the sparse and scattered cracks in Figure 11a; the roof remains virtually undamaged. Even when the excavation span is extended to 20 m, the limit for natural pillar support (Figure 10b), the roof deformation increases, yet the expandable prop load remains within the stable range, and the roof characteristic curve still intersects the expandable prop support curve at point *e* (lines ⑤ and ⑧ in Figure 9). At this span, the roof displacement is only 6.17 mm, still far below the 11.80 mm collapse displacement observed after natural pillar failure. Moreover, the roof cracks remain sparse and discontinuous (Figure 11b). The stope is therefore judged to remain stable. When the span is widened by 2 m on each side to 24 m, roof deformation surges and failure ensues. At this span, the support characteristic curve of the expandable prop (line ⑨ in Figure 9) still intersects the roof curve (line ⑥) at point *f*, but the roof has already entered the failure zone. At this stage, roof deflection reaches 8.24 mm, still less than the collapse displacement in the unsupported case, while cracks begin to coalesce at the abutments (Figure 11c).

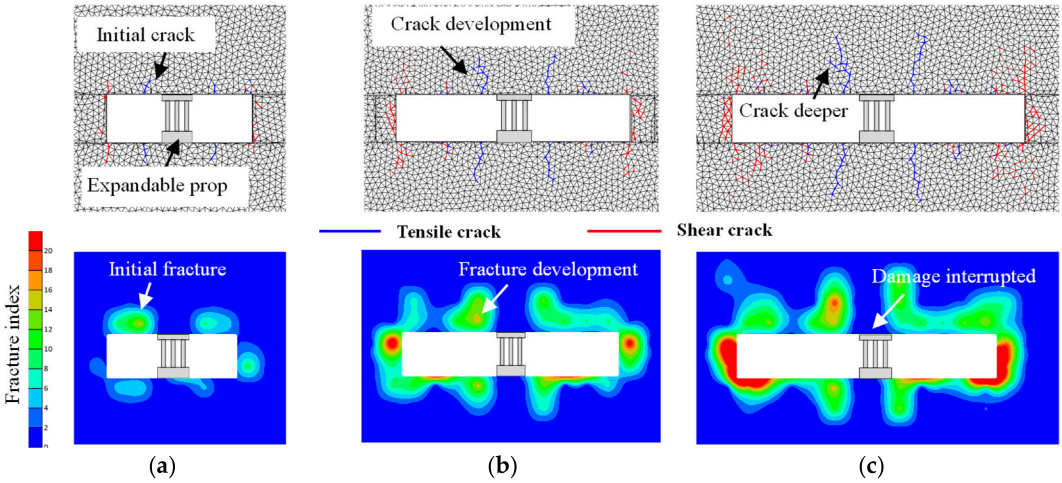



**Figure 11.** Final crack and fracture distribution supported by a single expandable prop support: (**a**) first excavation, (**b**) second excavation, and (**c**) third excavation.

Confined by the expandable prop, fractures propagate deeper instead of laterally, isolating a distinct failed zone in the roof. At a 12 m span, both the expandable prop and the natural pillar maintain roof stability, yet the prop permits larger roof deformation and carries markedly lower loads, clear evidence that it avoids rigid 'hard-top' restraint, allows stress relief, and delivers true yielding support. At a 20 m span, the natural pillar has reached its peak strength, whereas the expandable prop continues to provide reliable support, proving the effective span can be safely extended. Moreover, roof deformation beneath the expandable prop is far below the 11.8 mm collapse displacement observed after the natural pillar failed. This confirms that the expandable prop delivers true yielding support; even after the roof has undergone large stress-induced deformation, the prop sustains the load and preserves residual strength. Nevertheless, yielding support has its limits; excessive roof deformation in the absence of support can still precipitate instability.

### *5.2. Multiple Supports for a Single Stope*

#### 5.2.1. Natural Pillar Group

For the natural pillar group, the first excavation advance of 16 m yields the roof characteristic curve labeled ① in Figure 12. The mechanical response of natural pillar 1 is monitored, and its support characteristic curve ④ intersects the roof curve at point *g*, establishing equilibrium for the first excavation stage. Pillar 1 remains below its ultimate strength, showing only scattered cracks and a fracture index *D* of 15.5% (Figure 13(a1,a2)), still below the critical value of 20%. Advancing to the second step enlarges the span to 36 m, activating pillars 2 and 3. After re-equilibrating, pillar 1 retains a fracture index of 18.9%, still below the critical value of 20%, so it has not yet reached ultimate failure (Figure 13(b1,b2)). Pillars 2 and 3 begin carrying the overlying load within their respective bays. The roof characteristic curve ② intersects the collective support curve of the natural pillar group ⑤ at point *h* (Figure 12), while pillar 1 reaches its peak strength where its individual curve ④ meets line ② (Figure 12); equilibrium for the second stage is thereby established. Note that the stress–strain origin for pillars 2 and 3 is aligned with the horizontal coordinate of point a from the first-stage equilibrium; their curves are identical in shape to pillar 1's, differing only in the tributary roof area each pillar carries. Pillars 2 and 3 are partially ruptured (fracture index of 17–18%), while pillar 1 incurs further damage yet stays below the 20% threshold. A minor fissure opens at the stope roof center, but stability is maintained. Advancing to the third step, the span reaches 56 m. Pillars 4 and 5 engage and begin carrying the roof load. The roof characteristic curve ③ and the support characteristic curve of the natural pillar ⑥ intersect the point *I* (Figure 12), achieving equilibrium. Pillar 1 attains its limit strength (fracture index 22.9%, exceeding the 20% threshold), its support characteristic curve ④ no longer intersects the roof characteristic curve ③ (Figure 12) and the cracks develops (Figure 13(c1,c2)), and the pillar is removed from the model. After rebalancing, pillars 2 and 3 register maximum *D* values of 21.4%, surpassing the 20% limit, and are likewise deleted (Figure 13(d1,d2)). A continuous damage zone now spans the entire roof. After pillars 2 and 3 are removed, the model is re-equilibrated. Re-equilibration shows pillars 4 and 5 at *D* of 22.3%, again above the 20% limit, and they are therefore removed (Figure 13(e1,e2)). The continuous damage zone widens as cracks fully penetrate the roof. Bounded by pillars 4 and 5, the damage zone now blankets the entire roof (Figure 13(f1,f2)), signaling imminent full-scale collapse. The failure process of the natural pillar group exemplifies the 'domino effect' collapse.

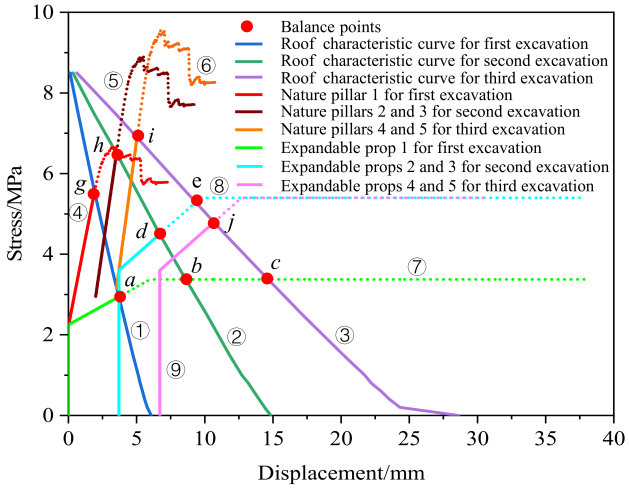



**Figure 12.** The relationship between the roof characteristic and support characteristic curves of natural pillar group and expandable prop group.

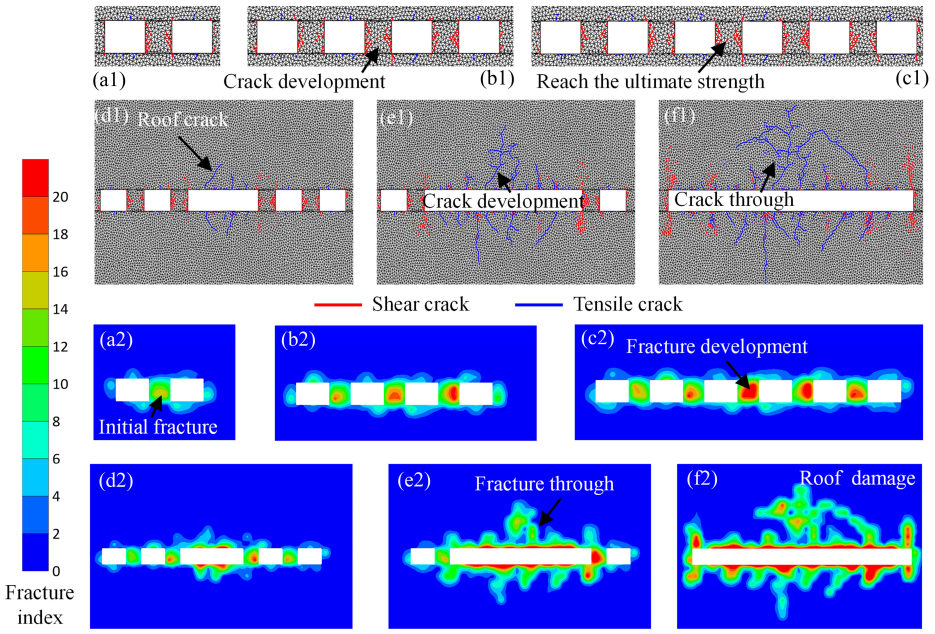



**Figure 13.** Final crack and fracture distribution supported by natural pillar group: (**a1**,**a2**) Excavation 1 balance. (**b1**,**b2**) Excavation 2 balance. (**c1**,**c2**) Excavation 3 balance. (**d1**,**d2**) Balance after removing pillar 1. (**e1**,**e2**) Balance after removing pillars 2 and 3. (**f1**,**f2**) Balance after removing pillars 4 and 5.

#### 5.2.2. Expandable Prop Group

After the first 16 m span is excavated, expandable prop 1 is activated and loaded; the roof characteristic curve ① intersects its support characteristic curve ⑦ at point *a* (Figure 12), establishing equilibrium. Expandable prop 1 records 17.6 mm axial displacement, well below its 50 mm limit, confirming stable support. Sparse cracks and fractures appear in the roof (Figure 14a), damage is minimal, and the stope remains stable. During the second advance to 36 m, expandable prop 1 remains stable; the roof characteristic curve ② intersects its support characteristic curve ⑦ at point *b* (Figure 12). Meanwhile, expandable props 2 and 3 are activated, and support characteristic curve ⑧ meets the roof characteristic curve ② for excavation stage 2 at point *d* (Figure 12). Expandable props 1, 2, and 3 register maximum axial displacements of 23.9 mm, still below the 50 mm limit, confirming continued stable support. At this stage, roof fracturing intensifies but remains non-penetrative, and tensile cracks dominate the central roof and propagate deeper, while shear fractures cluster along the sidewalls (Figure 14b), and the stable roof is stable. In the third advance, expandable prop 1 remains engaged; its support characteristic curve ⑦ meets the roof characteristic curve ③ at point *c* (Figure 12), and its load remains within the stable range. The support characteristic curve ⑧ of expandable props 2 and 3 meets the roof characteristic curve ③ at point *e* (Figure 12). Expandable props 4 and 5 are activated, and the support characteristic curve ⑨ meets the roof characteristic curve ③ at point *j* (Figure 12). Expandable prop 1 attains a peak axial displacement of 38.2 mm, while expandable props 2/3 and 4/5 reach maximum displacements of 34.2 mm and 23.9 mm, respectively, all comfortably below the 50 mm limit. After the third excavation, none of the expandable props have reached individual failure; tensile fractures in the stope roof remain centered and deepen, but not through, while shear fractures are confined to the sidewalls and previous excavation remnants, collectively indicating a stable roof (Figure 14c).

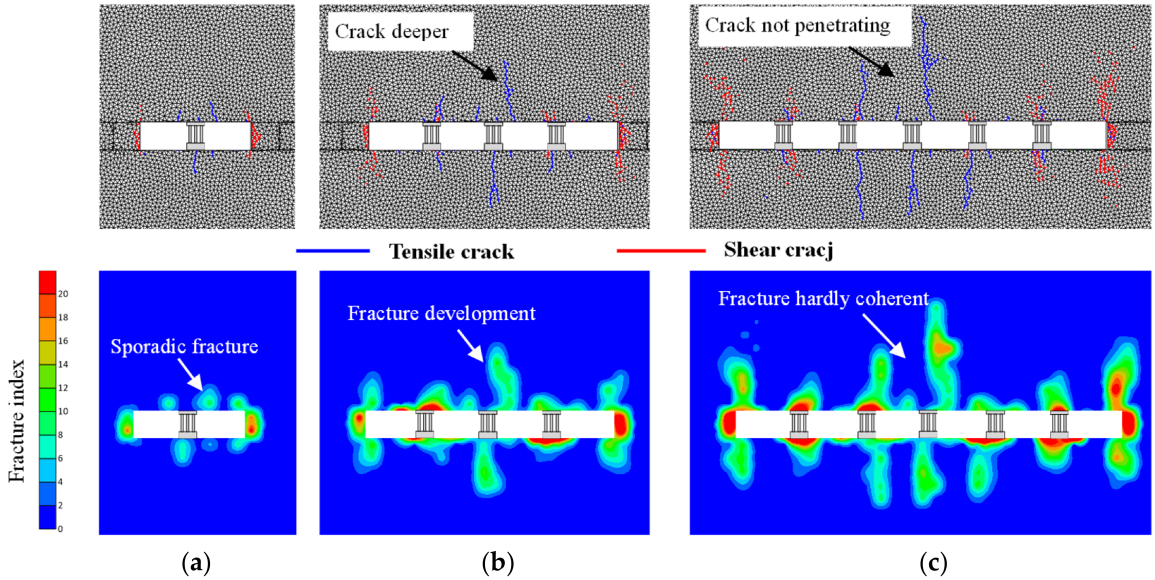


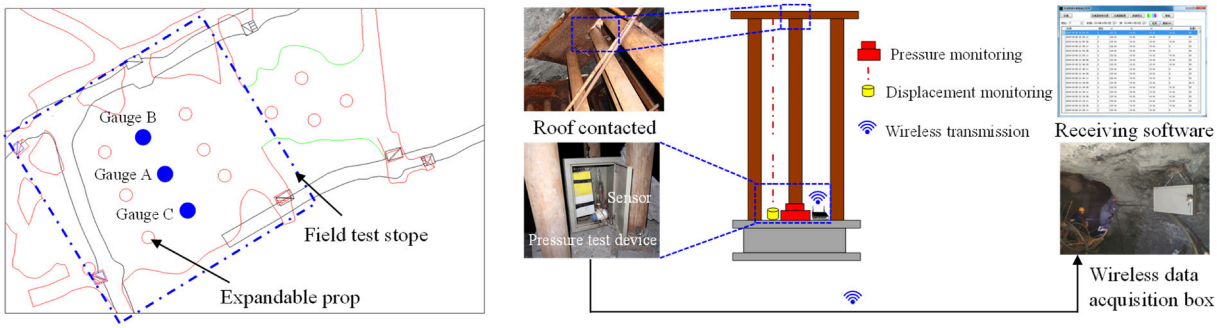

**Figure 14.** Final crack and fracture distribution supported expandable prop group: (**a**) after the first excavation, (**b**) after the second excavation, and (**c**) after the third excavation.

Overall, roof fractures and cracking localize almost entirely within natural pillars themselves, confirming that natural pillars act as stiff, self-supporting hard roofs. As the span widens, the failure of any overloaded pillar can trigger a rapid domino collapse. For expandable props, tensile cracks propagate downward, while shear cracks remain confined to the abutments, partitioning the damage zone and preventing load transfer between adjacent expandable props, effectively suppressing the domino effect. The expandable prop group delivers true yielding support, permitting greater roof deformation but requiring far lower support loads while maintaining the roof stability, which is an outcome unattainable with natural pillars. Ultimately, the expandable prop support system permits a markedly larger stope span while maintaining safety, far exceeding the limits achievable with the natural pillar support. Moreover, the robust residual strength of the expandable props interrupts damage propagation at wide spans, preventing the coalescence of fractured zones that would otherwise trigger domino damage inherent to natural pillar support. Even if domino failure eventually initiates in the expandable prop, its onset is far less abrupt and the safety margin markedly greater than with the natural pillars.

## 6. Field Industrial Test

### *6.1. On-Site Monitoring*

The room and expandable prop mining is executed for the horizontal thin veins of a gold mine in Dandong, China. As shown in Figure 15a, with the mining of the orebody, the expandable props are retained to support the stope roof. The mining and support sequence and the size of the stope are consistent with the numerical simulation. Mining is completed after installing three rows and three columns of expandable props, working from the interior of the stope outward. The support spacing of expandable props is 8 m. The bearing load of the expandable prop is measured with a custom pressure cake and laser-based wireless data loggers (Figure 15b). Three monitoring stations are installed in the stope, as shown in Figure 15a.




(**a**) (**b**)

**Figure 15.** On-site industrial test in room and expandable prop mining: (**a**) support and mining layout; (**b**) monitoring design.

### *6.2. Results and Analysis*

The expandable props generate an initial pre-stress of 1120 kN almost immediately after installation. Throughout mining, the load on expandable props continues to increase. Once the stope is fully mined, the expandable props maintain a stable bearing load. At this point, the central expandable prop (gauge A) carries a peak load of 1525 kN and a maximum vertical displacement of 5.1 mm. The loads and vertical displacements on the expandable props near the walls are relatively smaller. One expandable prop (gauge B) carries 1210 kN with 2.3 mm vertical displacement, while the other expandable prop (gauge C) carries 1175 kN and 2.5 mm vertical displacement. The loads and the displacements of expandable props do not all reach their limits of 2700 kN and 12 mm [15]. After the stope is mined, visually, the stope roof and expandable props appear to remain stable, as shown in Figure 16a. In contrast, stopes supported by natural pillars show splitting pillars and a collapsed roof (Figure 16b).



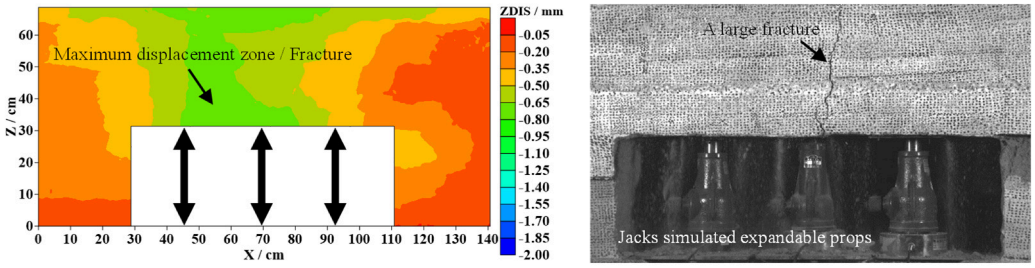

(**a**) (**b**)

**Figure 16.** The stability situation of the stope and the support bodies in the field: (**a**) expandable prop group support; (**b**) natural pillar group support.

## 7. Discussions

The numerical simulation shows that under expandable prop support, cracks extend into the deep roof but do not penetrate through it (Figure 14c), whereas the field trial exhibits no visible cracks due to a conservative, high-safety-margin design (Figure 16a). By contrast, the similar previously published laboratory test [51] reveals that under the support of the expandable props, as the roof is subjected to compression, initial cracks form in the center of the stope and continue to widen and extend, as shown in Figure 17, which is consistent with the results of numerical simulation. Therefore, the three outcomes are inherently consistent: the laboratory test captures the progressive crack development under continued loading, the numerical simulation shows that the expandable prop group

arrests crack penetration under controlled conditions, and the field trial demonstrates that an additional safety margin eliminates visible damage altogether. All confirm that the expandable prop group provides effective yielding support without compromising roof stability, avoiding the domino destruction phenomenon of natural ore pillars.




(**a**) (**b**)

**Figure 17.** Deformation and failure of the roof under the support of an expandable prop group: (**a**) displacement monitoring by DIC; (**b**) a large fracture in the stope roof [51].

The applicability of the proposed roof–support interaction framework is primarily associated with gently dipping and sub-horizontal thin-vein stopes supported by discrete natural pillars or expandable props. In the present study, the numerical model was established for a 4 m thick sub-horizontal orebody, and the rock mass and contact parameters were calibrated according to the corresponding engineering conditions. Therefore, the characteristic curves and quantitative results obtained in this study should not be directly transferred to substantially different geological and mining conditions. When applied to stopes with different mining depths, orebody thicknesses, in situ stress states, roof conditions, or rock mass properties, the mechanical parameters and roof–support characteristic curves should be recalibrated. Nevertheless, the proposed framework can still provide a general mechanical approach for evaluating the interaction between roof deformation and support resistance and for identifying the transition from stable equilibrium to progressive failure.

Several limitations of the present study should also be acknowledged. First, the UDEC-Trigon model is two-dimensional and cannot fully reproduce three-dimensional stress redistribution, out-of-plane roof deformation, or spatial interactions among support members. Second, the calibrated block-contact parameters represent the equivalent mechanical behavior of the rock mass under the geological conditions considered in this study, and their applicability to other rock masses requires additional calibration. Third, the support characteristic curve depends on the mechanical properties and working range of the specific expandable prop system adopted in this study; different prop types or structural parameters may lead to different roof–support interaction responses. Finally, the field verification was conducted under the geological and mining conditions of a single mine. Further three-dimensional numerical analyses and field investigations under different mining depths, stress conditions, roof qualities, and stope geometries are therefore required to assess the broader applicability of the proposed framework.

## 8. Conclusions

This study investigates the ground pressure control mechanism by which expandable prop groups stabilize the stope roof in room and expandable prop mining. Based on theoretical analysis, UDEC-Trigon numerical simulation, and field verification, the following conclusions are drawn:

(1) The calibrated UDEC-Trigon model satisfactorily reproduces the principal macroscopic mechanical properties of the target rock mass. The relative errors of the uniaxial

compressive strength, Young's modulus, and tensile strength are 1.25%, −2.14%, and 3.68%, respectively. The MAPE and RMSRE are 2.36% and 2.56%, respectively, and the maximum absolute relative error is 3.68%, providing a quantitative basis for the subsequent analysis of roof–support interaction and progressive failure.

(2) Natural pillars behave as relatively rigid supports, causing stress and damage to concentrate within the pillars. With increasing excavation span, the fracture index of pillar 1 reaches 22.9%, exceeding the 20% failure threshold. Following its failure, the maximum fracture indices of pillars 2–3 and pillars 4–5 increase to 21.4% and 22.3%, respectively, resulting in progressive load transfer, fracture coalescence, and, ultimately, a domino-type failure of the natural pillar group and stope roof.

(3) Expandable prop groups exhibit a markedly different roof-control mechanism. They accommodate roof deformation while maintaining continuous load-bearing capacity, thereby redistributing damage toward the deeper roof and abutments and inhibiting fracture coalescence. During the final excavation stage, the maximum axial displacements of expandable prop 1, props 2–3, and props 4–5 are 38.2, 34.2, and 23.9 mm, respectively, all below the 50 mm numerical displacement limit. The roof fractures remain non-penetrating, demonstrating the yielding-support mechanism of the expandable prop group.

(4) Field monitoring further supports the numerical results. The expandable props provide an initial pre-stress of approximately 1120 kN. After the completion of mining, the measured loads at gauges A, B, and C are 1525, 1210, and 1175 kN, respectively, with corresponding vertical displacements of 5.1, 2.3, and 2.5 mm. These values remain below the adopted bearing-load and displacement limits of 2700 kN and 12 mm. Under the tested geological and mining conditions, the expandable prop group therefore maintained stable roof support throughout the monitored mining process.

Future research will focus on extending the present roof–support interaction framework in three aspects. First, three-dimensional numerical models will be developed to investigate the coupled mechanical interaction among the stope roof, expandable prop group, and backfill, including spatial load transfer and out-of-plane deformation that cannot be fully represented by the present two-dimensional model. Second, systematic parametric analyses will be conducted to quantify the effects of mining depth, stope span, rock mass properties, initial pre-stress, prop spacing, and yielding capacity on the roof–support characteristic curves, with the aim of developing more general design criteria for expandable prop groups. Third, additional field monitoring and engineering applications under different geological and mining conditions will be carried out to further evaluate the transferability and long-term performance of the proposed yielding-support framework.

**Author Contributions:** K.L.: Conceptualization, Methodology, Funding Acquisition, Validation, Writing—Original Draft, and Writing—Review and Editing. Y.L.: Methodology, Validation, and Writing—Reviewing and Editing. Z.F.: Methodology, Validation, and Writing—Reviewing and Editing. J.L.: Validation and Writing—Reviewing and Editing. Y.W.: Writing—Reviewing and Editing. X.W.: Writing—Reviewing and Editing. All authors have read and agreed to the published version of the manuscript.

**Funding:** This work was financially supported by the National Natural Science Foundation of China (Grant No. 52374117), the Central Government Guided Local Science and Technology Development Fund Projects (Grant No. 2026JH6/101000028), and the Science and Technology Projects of Inner Mongolia Autonomous Region (Grant No. 2025YFDZ0013), and Excellent Research Team Construction Project—Excellent Youth Science and Technology Talent Cultivation Project (N26QNR008).

**Institutional Review Board Statement:** Not applicable.

**Informed Consent Statement:** Not applicable.

**Data Availability Statement:** The raw data supporting the conclusions of this article will be made available by the authors on request.

**Conflicts of Interest:** Author Zhengchun Fu was employed by the company Hunan Research Institute for Nonferrous Metals Co., Ltd. The remaining authors declare that the research was conducted in the absence of any commercial or financial relationships that could be construed as a potential conflict of interest.

## Abbreviations and Symbols

| | |
|---|---|
| UDEC | Universal Distinct Element Code |
| FEM | Finite element method |
| FDM | Finite difference method |
| DEM | Discrete element method |
| DIC | Digital image correlation |
| $S_V$ | Vertical in situ stress |
| $S_H$ | Horizontal in situ stress |
| $S_{V\text{-top}}$ | Vertical stress at the upper boundary of the numerical model |
| $S_{V\text{-roof}}$ | Initial vertical stress at the stope roof |
| $\rho$ | Density of rock mass |
| $g$ | Gravitational acceleration |
| $\gamma$ | Unit weight of rock mass |
| $H$ | Burial depth |
| $E$ | Young's modulus |
| $\nu$ | Poisson's ratio |
| $c$ | Cohesion |
| $\varphi$ | Friction angle |
| $\sigma_c$ | Uniaxial compressive strength |
| $\sigma_t$ | Tensile strength |
| $k_n$ | Normal contact stiffness |
| $k_s$ | Shear contact stiffness |
| $\sigma_n$ | Normal stress on a contact |
| $\tau_s$ | Shear stress on a contact |
| $\tau_{max}$ | Maximum shear strength of a contact |
| $c_j$ | Contact cohesion |
| $\varphi_j$ | Contact friction angle |
| $\sigma_{tj}$ | Contact tensile strength |
| $p_s$ | Equivalent support pressure |
| $\sigma_p$ | Axial stress of the natural pillar |
| $A_p$ | Cross-sectional area of the natural pillar |
| $A_t$ | Tributary roof area supported by the pillar |
| $D$ | Fracture index |
| $L_s$ | Cumulative length of shear cracks |
| $L_t$ | Cumulative length of tensile cracks |
| $L_c$ | Total length of block contacts |

## References

1. Tian, C.Y.; Luo, S.H.; Wu, Y.P.; Xie, P.S.; Wang, H.W.; Cheng, H.F.; Yan, Z.Z. Rock pillar fracture-induced vibration characteristics and rock burst mechanism in steeply inclined extra-thick coal seam group mining. *Appl. Sci.* **2026**, *16*, 8198. [CrossRef]
2. Li, K.; Fu, Z.C.; Li, J.T.; Li, Y.H.; Zhang, J.Q.; Chen, L. Fracturing rocks using expandable materials for steeply inclined thin vein mining. *J. Rock Mech. Geotech. Eng.* **2026**, *18*, 6122–6134. [CrossRef]
3. Guo, L.J.; Tao, Z.G.; He, M.C.; Coli, M. Impact of Micro-NPR bolt on the mining of deep-buried phosphate via the room-and-pillar method. *Tunn. Undergr. Space Technol.* **2023**, *140*, 105326. [CrossRef]

4. Chen, T.X.; Xu, S.D.; He, B.G.; Li, Y.H.; Peng, J.Y. Study on the relationship between surface deformation and internal fracturing of tunnel surrounding rock under uniaxial loading with multiple blasting disturbances. *Tunn. Undergr. Space Technol.* **2026**, *173*, 107646. [CrossRef]
5. Guo, Y.H.; Miao, Y.C. Study on stope sability in continuous mining of long-dip, thin orebody by room-pillar method. *Sustainability* **2022**, *14*, 9601. [CrossRef]
6. Shnorhokian, S.; Mitri, H.S.; Moreau-verlaan, L. Stability assessment of stope sequence scenarios in a diminishing ore pillar. *Int. J. Rock Mech. Min. Sci.* **2015**, *74*, 103–118. [CrossRef]
7. Wang, J.A.; Shang, X.C.; Ma, H.T. Investigation of catastrophic ground collapse in Xingtai gypsum mines in China. *Int. J. Rock Mech. Min. Sci.* **2008**, *45*, 1480–1499. [CrossRef]
8. Cao, S.; Xue, G.L.; Yilmaz, E.; Yin, Z.Y.; Yang, F.D. Utilizing concrete pillars as an environmental mining practice in underground mines. *J. Clean. Prod.* **2021**, *278*, 123433. [CrossRef]
9. Peng, F.H.; Wang, W.J. Experimental study and engineering application of concrete-encased reinforcement for mine pillars. *Appl. Sci.* **2025**, *15*, 10615. [CrossRef]
10. Barczak, T.M. An overview of standing roof support practices and developments in the United States. In *Proceedings of the Third South African Rock Engineering Symposium, Johannesburg, South Africa*; South African Institute of Mining and Metallurgy: Johannesburg, South Africa, 2005; pp. 301–334.
11. Ullah, M.F.; Alamri, A.M.; Mehmood, K.; Akram, M.S.; Rehman, F.; Rehman, S.U.; Riaz, O. Coal mining trends, approaches, and safety hazards: A brief review. *Arab. J. Geosci.* **2018**, *11*, 651. [CrossRef]
12. Timothy, B. Analysis of the design and performance characteristics of pumpable roof supports. *Int. J. Min. Sci. Technol.* **2017**, *27*, 91–99. [CrossRef] [PubMed]
13. Sun, L.H.; Wu, H.Y.; Yang, B.S.; Li, Q.Q. Support failure of a high-stress soft-rock roadway in deep coal mine and the equalized yielding support technology: A case study. *Int. J. Coal Sci. Technol.* **2015**, *2*, 279–286. [CrossRef]
14. Li, Y.H.; Li, K.M.; Feng, X.T.; Cai, M. Development and evaluation of artificial expandable pillars for hard rock mining. *Int. J. Rock Mech. Min. Sci.* **2018**, *110*, 68–75. [CrossRef]
15. Li, K.M.; Jiang, K.Y.; Li, Y.H.; Wang, X.; Liu, K.; Xu, S. Determination of the load bearing capacity of pre-stressed expandable props for ground support in underground mines. *Int. J. Min. Sci. Technol.* **2023**, *33*, 977–990. [CrossRef]
16. Chen, D.D.; Chang, J.C.; Zou, J.; Tian, C.Y.; Xie, S.R.; Ni, J.; Guo, F.F.; Zhang, Z.X.; Zhao, W.K.; Yang, X.Y.; et al. Mechanisms of surrounding rock failure and control measures when main roof fractures directly above gob-side entry in thick coal seam. *Appl. Sci.* **2025**, *15*, 4284. [CrossRef]
17. Bednarek, Ł.; Małkowski, P.; Niedbalski, Z.; Mucha, K. Steel arch and rock bolt support in terms of the gateroad stability maintaining behind the longwall face. *Appl. Sci.* **2024**, *14*, 3594. [CrossRef]
18. Hou, P.; Kong, K.; Wang, X.; Li, J.; Han, M.; Cai, M. A new dilation angle model and a cohesion-weakening and friction-weakening model for simulating post-peak deformation of brittle hard rocks. *J. Rock Mech. Geotech. Eng.* **2026**, *18*, 2530–2545. [CrossRef]
19. Xu, S.D.; Chen, T.X.; He, B.G.; Li, Y.H. Study of the relationship between the attenuation pattern of acoustic emissions and stress levels after a blasting disturbance. *Rock Mech. Rock Eng.* **2025**, *58*, 10085–10103. [CrossRef]
20. Kujoana, M.A. Quest for 'effective pack' support. *J. South. Afr. Inst. Min. Metall.* **2009**, *109*, 233–238.
21. Li, K.M.; Li, Y.H.; Wang, Z.C.; Xu, S.; Xiong, Z.P. Research on the enlargement of stope span based on the pre-stressed expandable pillar support technology. *Rock Mech. Rock Eng.* **2021**, *54*, 4663–4675. [CrossRef]
22. Schubert, W. Dealing with squeezing conditions in Alpine tunnels. *Rock Mech. Rock Eng.* **1996**, *29*, 145–153. [CrossRef]
23. Moritz, A.B. Ductile Support System for Tunnels in Squeezing Rock. Doctoral Thesis, Graz University of Technology, Graz, Austria, 1999.
24. Kolymbas, D. Stress and deformation fields around a deep circular tunnel. In *Tunnelling and Tunnel Mechanic: A Rational Approach to Tunnelling*; Springer: Berlin/Heidelberg, Germany, 2005; pp. 273–306.
25. Weidinger, F.; Lauffer, H. The Tauern tunnel first and second tubes from the contractor's viewpoint. *Geomech. Tunn.* **2009**, *2*, 24–32. [CrossRef]
26. Moritz, B. Überblick und vergleich. *Geomech. Tunn.* **2011**, *4*, 221–236. [CrossRef]
27. Thut, A.; Naterop, D.; Steiner, P.; Stolz, M. Tunnelling in squeezing rock-yielding elements and face control. In Proceedings of the 8th International Conference on Tunnel Construction and Underground Structures, Ljubljana, Slovenia, 15–17 November 2006; pp. 221–241.
28. Merlini, D.; Stocker, D.; Falanesca, M.; Schuerch, R. The ceneri base tunnel: Construction experience with the southern portion of the flat railway line crossing the swiss alps. *Engineering* **2018**, *4*, 235–248. [CrossRef]
29. Hoek, E.; Guevara, R. Overcoming squeezing in the Yacambú-Quibor tunnel, Venezuela. *Rock Mech. Rock Eng.* **2009**, *42*, 389–418. [CrossRef]
30. Panet, M. Two case histories of tunnels through squeezing rocks. *Rock Mech. Rock Eng.* **1996**, *29*, 155–164. [CrossRef]

31. Barla, G.; Bonini, M.; Semeraro, M. Analysis of the behaviour of a yield-control support system in squeezing rock. *Tunn. Undergr. Space Technol.* **2011**, *26*, 146–154. [CrossRef]
32. Mezger, F.; Ramoni, M.; Anagnostou, G. Options for deformable segmental lining systems for tunnelling in squeezing rock. *Tunn. Undergr. Space Technol.* **2018**, *76*, 64–75. [CrossRef]
33. Dalgıç, S. Tunneling in squeezing rock, the Bolu tunnel, Anatolian Motorway, Turkey. *Eng. Geol.* **2002**, *67*, 73–96. [CrossRef]
34. Kimura, F.; Okabayashi, N.; Kawamoto, T. Tunnelling through squeezing rock in two large fault zones of the Enasan Tunnel II. *Rock Mech. Rock Eng.* **1987**, *20*, 151–166. [CrossRef]
35. Zhang, Z. Discussion and study on large deformation of tunnel in squeezing ground. *Mod. Tunn. Technol.* **2003**, *40*, 5–12.
36. Zhang, B.; Zhang, Z.Q.; Wang, B.; Zhou, L. Experimental study of application of yielding bolt to large deformation tunnel. *Rock Soil Mech.* **2016**, *37*, 2047–2055.
37. Tan, X.J.; Chen, W.Z.; Liu, H.Y.; Chan, A.H.C.; Tian, H.M.; Meng, X.J.; Wang, F.Q.; Deng, X.L. A combined supporting system based on foamed concrete and U-shaped steel for underground coal mine roadways undergoing large deformations. *Tunn. Undergr. Space Technol.* **2017**, *68*, 196–210. [CrossRef]
38. Qiu, W.G.; Wang, G.; Gong, L.; Shen, Z.; Li, C.; Dang, J. Research and application of resistance-limiting and energy-dissipating support in large deformation tunnel. *Chin. J. Rock Mech. Eng.* **2018**, *37*, 1785–1795.
39. Li, Q.; Wu, G.Y.; Kong, D.Z.; Han, S.; Ma, Z.Q. Study on mechanism of end face roof leaks based on stope roof structure movement under repeated mining. *Eng. Fail. Anal.* **2022**, *135*, 106162. [CrossRef]
40. Lu, J.; Jiang, C.B.; Jin, Z.; Wang, W.S.; Zhuang, W.J.; Yu, H. Three-dimensional physical model experiment of mining-induced deformation and failure characteristics of roof and floor in deep underground coal seams. *Process Saf. Environ. Prot.* **2021**, *150*, 400–415. [CrossRef]
41. Bai, J.B.; Shen, W.L.; Guo, G.L.; Wang, X.Y.; Yu, Y. Roof deformation, failure characteristics, and preventive techniques of gob-side entry driving heading adjacent to the advancing working face. *Rock Mech. Rock Eng.* **2015**, *48*, 2447–2458. [CrossRef]
42. Kong, D.Z.; Li, Q.; Wu, G.Y.; Song, G.F. Characteristics and control technology of face-end roof leaks subjected to repeated mining in close-distance coal seams. *Bull. Eng. Geol. Environ.* **2021**, *80*, 8363–8383. [CrossRef]
43. Liu, J.H.; Bai, J.; Wang, Q.; Zhang, F.; Liu, S.; Wang, X.; Yan, S. Failure mechanism and support control of deep gob-side entry retaining in top-coal roadways. *Appl. Sci.* **2025**, *16*, 7390. [CrossRef]
44. Sinha, S.; Abousleiman, R.; Walton, G. Effect of damping mode in laboratory and field-scale universal distinct element code (UDEC) models. *Rock Mech. Rock Eng.* **2022**, *55*, 2899–2915. [CrossRef]
45. Gao, F.Q.; Stead, D. The application of a modified Voronoi logic to brittle fracture modelling at the laboratory and field scale. *Int. J. Rock Mech. Min. Sci.* **2014**, *68*, 1–14. [CrossRef]
46. Brown, E.T.; Hoek, E. Trends in relationships between measured in situ stresses and depth. *Int. J. Rock Mech. Min. Sci. Geomech. Abstr.* **1978**, *15*, 211–215. [CrossRef]
47. Mu, Z.L.; Ji, J.Q.; Cao, J.L.; Shi, M.N.; Zhuang, J.X.; Jiang, C.L.; Li, J.X. Study on surface damage induced by high heavy layer movement and mining-induced earthquakes. *Appl. Sci.* **2025**, *15*, 6577. [CrossRef]
48. Wang, Y.C.; Chen, P.K.; Wang, S. Study of overlying rock structure and intensive pressure control technology of island longwall panel in extra-thick coal seams. *Processes* **2023**, *11*, 3083. [CrossRef]
49. Tang, Y.; Yang, J.H.; You, Y.Y.; Fu, J.Y.; Zheng, X.C.; Zhang, C. Multi-output prediction for TBM operation parameters based on stacking ensemble algorithm. *Tunn. Undergr. Space Technol.* **2024**, *152*, 105960. [CrossRef]
50. Wang, R.; Wang, Y.; Yan, B.; Yoshitake, I.; Ding, B.S. Three-dimensional numerical simulation method for shield grouting based on DEM-FDM coupling and inlet module. *Tunn. Undergr. Space Technol.* **2025**, *165*, 106858. [CrossRef]
51. Li, K.M.; Wang, Y.J.; Liu, K.; Li, Y.H.; Fu, Z.C.; Pang, B.X. Determination of support mechanical mechanism of pre-stressed expandable props to stope roof in room-and-pillar mining. *J. Cent. South Univ.* **2025**, *32*, 3539–3556. [CrossRef]


**Disclaimer/Publisher's Note:** The statements, opinions and data contained in all publications are solely those of the individual author(s) and contributor(s) and not of MDPI and/or the editor(s). MDPI and/or the editor(s) disclaim responsibility for any injury to people or property resulting from any ideas, methods, instructions or products referred to in the content.